A NUMERICAL VIRTUAL FLIGHT PLATFORM DEVELOPMENT AND ITS APPLICATION ON HIGH MANEUVERABILITY FLIGHT VEHICLES

Hongyu QIAO[1], Fan QIN[1], Shuanghou DENG[1]

[1] Nanjing University of Aeronautics and Astronautics, 210016, Nanjing, P.R. China

Abstract

In order to address the intricate flow phenomena and multidisciplinary coupling effects of highly maneuverable aircraft, this study develops a numerical virtual flight platform that integrates an unsteady flow solver, rigid body dynamics solver, and flight control system module. The IRIS-T missile is chosen as the simulation object for conducting numerical virtual flight simulations of high angle of attack pull-up maneuvers and roll maneuvers. The experimental results demonstrate that this technique accurately captures the characteristics and response patterns of the missile during maneuvering flights, thereby providing essential insights for practical aircraft design and analysis.

Keywords: High maneuverability aircraft, Numerical virtual flight, Aerodynamic-motion-control coupling

1. Research background

High maneuverability and exceptional stall recovery capability are indispensable attributes of high-performance aircraft, enabling them to gain a tactical advantage in combat scenarios and augment their overall combat effectiveness. However, these capabilities also present significant challenges in terms of aircraft design and control. When an aircraft maneuvers at high angles of attack, its attitude angle, angular velocity, and angular acceleration undergo substantial changes, while pronounced flow separation induces unsteady and nonlinear variations in the aerodynamic and kinematic parameters of the aircraft. Consequently, intricate multidisciplinary coupling phenomena arise among aerodynamics, kinematics, elasticity, and control systems. These phenomena can give rise to nonlinear motions such as inertial coupling effects, wing oscillations (wing rock), deep stalls, or tailspins. Conventional virtual flight test technologies like wind tunnel-based simulations may not adequately capture these complex flow phenomena or account for the multidisciplinary coupling effects encountered during actual flight conditions due to limitations pertaining to cost-effectiveness, time constraints accuracy levels as well as scalability issues [1].

To tackle these challenges, numerical virtual flight has emerged as a more dependable solution due to the rapid advancements in CFD numerical solution technology, grid generation technology, and large-scale parallel computing. Numerical virtual flight offers advantages such as refinement, high speed, cost-effectiveness, and multidisciplinary integration [2]. For highly maneuverable aircraft, this technology can overcome the limitations of existing virtual flight test methods by capturing complex flow phenomena and multidisciplinary coupling effects encountered during actual flights. By evaluating and enhancing the flight control system for fast maneuverable flights, this approach can improve the performance of virtual flight experiments [3]. Consequently, it enables a shift from traditional "test-flight-and-improvement" models to integrated multidisciplinary design models [4].

At present, many researches have been carried out on virtual flight of high mobility aircraft in the industry: NASA Ames Research Center conducted a project on the Virtual Flight Rapid Integration

Test Environment [5], CFD, flight and wind tunnel data can be integrated into simulation data to evaluate the role of driving simulations in the conceptual design of advanced aircraft. Paul Weinacht [6] coupled CFD, guidance, navigation and control, and structural dynamics, and used closed-loop feedback control with integral control to obtain the command canard deflection, and studied the performance of the smart material canard actuator. M.R.Allan et al. [7] used the parallel multi-block RANS solver from the University of Glasgow in 2005 to numerically simulate the longitudinal motion of a general-purpose fighter shape, and incorporated the flight mechanics equation and controller into the CFD solution loop to analyze the pitch motion process of the aircraft with one degree of freedom and three degrees of freedom considering the deflection of the control surface. Bradford E. Green [8] used Kestrel solver to analyze the stability and control characteristics of F/A-18E fighter aircraft and E-2D aircraft [9], and compared the results with wind tunnel data, flight database data or known data trends to verify the accuracy of the software. Jubaraj Sahu et al. [10, 11] used CFD++ solver to perform time-precise coupled CFD/RBD virtual flight calculation for canard winged missiles. On this basis, CFD/RBD/FCS coupling method was adopted, that is, the canard wing deflection output of flight control components was used for mesh deformation. For the calculation of the next CFD time step, the aerodynamic torque calculated by CFD determines the flight motion of the missile and the control deflection of the canard wing, simulating the flight motion of the missile. In 2016, C. Justin Ratcliff et al. [12] studied the virtual flight test capability of incorporating pilot model, F-16 flight control system (FLCS) and six-degree-of-freedom motion calculation into CFD maneuver simulation. The Cobalt solver with MATLAB/Simulink external control interface is used to carry out virtual flight test on the full-size F-16C aircraft, and the accuracy of the calculation is verified.

2. Technical method

To address the issue of tight coupling between aerodynamics and motion during high maneuvering flight of aircraft, this study presents a numerical virtual flight simulation platform for integrated aerodynamic-motion-control coupling based on an advanced solver for complex aerodynamic simulations. The platform employs an unsteady airflow numerical solution method, unstructured nested grid technology, and flight mechanics equation numerical solution method. Additionally, it incorporates the design of an aircraft attitude control system to establish seamless integration between the control system and solver. The key technical methods involved are as follows:

2.1 CFD numerical solution method

The CFD grid division employs dynamic unstructured nested grid technology, which partitions the aircraft's flow field into multiple regions with overlapping components. Each region generates independent grids and solves them individually [13]. An interpolation method is employed to establish a relationship between the grids, facilitating information exchange of the flow field across different grids.

The CFD numerical solution method utilizes the mature and reliable three-dimensional unsteady Reynolds averaged N-S (RANS) equation to calculate both static and dynamic data of the simulated model. For spatial discretization, a finite volume approach is adopted for unsteady compressible flow calculations. Pseudo time step first-order backward difference is used for time step discretization, while implicit second-order backward difference format is employed for physical time step discretization due to its stability, faster convergence speed, and efficiency—particularly in viscous flow field calculations. Additionally, in order to close the RANS equation, an S-A (Spalart-Allmaras) turbulence model is introduced to simulate Reynolds stress terms.

2.2 Flight mechanics equation numerical solution method

Nonlinear six-degree-of-freedom motion equation is the basic equation of aircraft motion, in which six dynamic equations describe the motion of center of mass and the rotation of aircraft around center of mass, and six kinematic equations describe the change of position and attitude of aircraft in space. Assuming that the aircraft is a rigid body and its mass is constant, its dynamic equation is as follows:

$$\begin{cases} \dot{u} = vr - wq - g\sin\theta + \dfrac{F_x}{m} \\ \dot{v} = -ur + \omega p + g\cos\theta\sin\phi + \dfrac{F_y}{m} \\ \dot{\omega} = uq - vp + g\cos\theta\cos\phi + \dfrac{F_z}{m} \\ \dot{p} = (c_1 r + c_2 p)q + c_3 L + c_4 N \\ \dot{q} = c_5 pr - c_6(p^2 - r^2) + c_7 M \\ \dot{r} = (c_8 p - c_2 r)q + c_4 L + c_9 N \end{cases} \tag{1}$$

Where, (*u, v, w*) are the components of the flight speed on the three axes, respectively; (*p, q, r*) are the components of the rotational angular velocity of the aircraft on each axis of the body coordinate system, respectively are the roll angle velocity, pitch angle velocity and yaw angular velocity; (*Fx, Fy, Fz*) as the effect on the aircraft outside force vector of the projection on the component in dynamic systems, θ and ϕ pitch angle and roll angle respectively; (*L, M, N*) is the component of aerodynamic torque received by the aircraft on the coordinate axis, which are respectively rolling moment, pitching moment and yaw moment. Coefficients *c1~c9* in Equation (1) are respectively expressed as:

$$c_1 = \frac{(I_y - I_z)I_z - I_{xz}^2}{I_x I_z - I_{xz}^2}, \quad c_2 = \frac{(I_x - I_y + I_z)I_{xz}}{I_x I_z - I_{xz}^2}, \quad c_3 = \frac{I_z}{I_x I_z - I_{xz}^2}, \quad c_4 = \frac{I_{xz}}{I_x I_z - I_{xz}^2},$$

$$c_5 = \frac{I_z - I_x}{I_y}, \quad c_6 = \frac{I_{xz}}{I_y}, \quad c_7 = \frac{1}{I_y}, \quad c_8 = \frac{I_x(I_x - I_y) + I_{xz}^2}{I_x I_z - I_{xz}^2}, \quad c_9 = \frac{I_x}{I_x I_z - I_{xz}^2}$$

The kinematics equation of the aircraft is:

$$\begin{cases} \dot{\phi} = p + \tan\theta(q\sin\phi + r\cos\phi) \\ \dot{\theta} = q\cos\phi - r\sin\phi \\ \dot{\psi} = \dfrac{1}{\cos\theta}(q\sin\phi + r\cos\phi) \\ \dot{x}_g = V\cos\mu\cos\varphi \\ \dot{y}_g = V\cos\mu\sin\varphi \\ \dot{h} = V\sin\mu \end{cases} \tag{2}$$

Where, (ϕ, θ, ψ) flying roll angle and pitching angle and yaw angle respectively, *V* flight speed.

In this paper, the fourth-order Runge-Kutta method is used to solve the parameters such as angular velocity, Euler angle and position at a given time. The calculation formula is as follows:

$$x(t+T) = x(t) + T\sum_{i=1}^{4} c_i k_i \tag{3}$$

2.3 Aircraft control system design method

In this paper, a combination algorithm of discrete positional PID and incremental PID control algorithm is adopted, as shown in the figure 1. This algorithm discretized the traditional PID method, with sampling moment point *kT* representing continuous time, numerical integration replacing integration by matrix method, and first-order backward difference replacing differential, the discretized positional PID expression can be obtained as follows:

$$\begin{aligned} u(k) &= k_p\left(e(k) + \frac{T}{T_i}\sum_{j=0}^{k} e(j) + \frac{T_D}{T}(e(k) - e(k-1))\right) \\ &= k_p e(k) + k_i\sum_{j=0}^{k} e(j)T + k_d\frac{e(k) - e(k-1)}{T} \end{aligned} \tag{4}$$

In order to avoid error accumulation of integral term of position-type PID, the expression of discrete incremental PID is adopted as follows:

$$\begin{aligned}\Delta u(k) &= u(k) - u(k-1) \\ &= k_p(e(k) - e(k-1)) + k_i e(k) + k_d(e(k) - 2e(k-1) + e(k-2))\end{aligned} \tag{5}$$

Where,

$$u(k-1) = k_p e(k-1) + k_i \sum_{j=0}^{k-1} e(j) + k_d(e(k-1) - e(k-2))$$

$$u(k) = k_p e(k) + k_i \sum_{j=0}^{k} e(j) + k_d(e(k) - e(k-1))$$

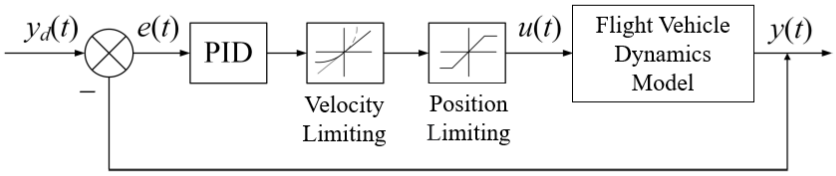

Figure 1 – Schematic diagram of missile attitude control system

Simultaneously, due to limitations on the deflection rate and angle of the aircraft control surface, there are corresponding restrictions on the speed and angle of deflection. Consequently, the control surface speed and deflection angle can only fall within a specified range to prevent saturation of the integral term in position-type PID control.

The sampling frequency for this system is determined based on its closed-loop frequency bandwidth. As a closed-loop system, the flight control system inherently exhibits low-pass filtering characteristics, thereby suppressing motion modes with amplitudes higher than the system's frequency band through attenuation. The selected sampling frequency should be 4-10 times greater than the loop's closed-loop bandwidth [14].

The parameters for PID controller are obtained using critical proportionality method. Initially, only proportional gain is applied to the controlled object while setting integral and derivative coefficients as zero; subsequently, by gradually increasing proportional gain from small to large values until achieving equal amplitude oscillation in step response output of the system, we can determine critical proportionality (Kcr) and corresponding oscillation period (Tcr). Finally, empirical formulas are used to calculate PID control parameters which can then be adjusted according to specific control objectives.

3. CFD/RBD/FCS coupling technical method

According to the aforementioned technical methods, this paper presents a numerical virtual flight platform for high maneuvering aircraft that integrates key technologies such as CFD numerical solution method, flight mechanics equation numerical solution method, and flight control system design method.

The platform operation process is shown in Figure 1. For different simulation models, the platform calculates the initial flow field based on the set external environment and obtains static and dynamic aerodynamic characteristics parameters of the aircraft. It establishes a transfer function between the aircraft attitude angle and control surface deflection angle using these parameters to design the control system. Subsequently, an iterative solution is initiated in the simulation platform.

In each iteration, first, it calculates the unsteady flow field of the aircraft to determine its aerodynamic

force and moment at current time. Then, employing fourth-order Runge-Kutta method, it computes six-degree-of-freedom motion equations using these forces and moments to obtain motion parameters like Euler angles, angular velocity, force vectors, and moment tensors of the aircraft model. The control module compares these obtained motion parameters with target values according to predefined objectives and determines controlled sub-grid displacements based on specified control parameters. Using dynamic grid generation technology along with Euler angles from six-degree-of-freedom motion module and displacements from control module; grid motion module updates sub-grid coordinates accordingly for solving at next time step. Thusly completing a numerical virtual flight involving integrated coupling of aerodynamics-motion-control which proceeds iteratively until accomplishing entire solution process.

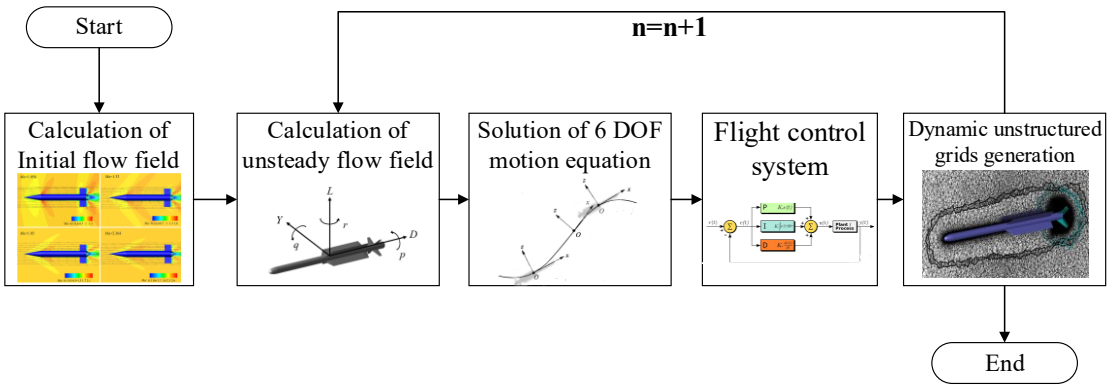

Figure 2 – High maneuverability flight vehicles numerical virtual flight flow chart

4. Application of Numerical Virtual Flight Platform for High Maneuvering Aircraft

In this virtual simulation, the narrow-wing layout missile IRIS-T is utilized as the simulation model, as depicted in Figure 3. The IRIS-T missile weighs approximately 89kg and measures 2.94m in length with a body diameter of 127mm. It achieves a maximum flight speed of Mach 3. Considering its maneuvering characteristics, there exists no fundamental distinction between its pitch and yaw motion during extensive maneuvers; thus, its pitch and roll attributes significantly impact its performance. This paper conducts numerical simulations on both longitudinal high angle of attack pull-up maneuvers and lateral roll maneuvers using the CFD/RBD/FCS coupling high maneuvering aircraft's numerical virtual flight platform.

Based on the IRIS-T missile model, unstructured nested grids are employed for CFD grid division with conical far field boundaries shown in Figure 4. The grid configuration comprises six sets: one background grid, one body grid, and four control surface grids. The body and control surface grids establish nested relationships with the background grid individually to enable control over missile attitude angles by adjusting deflection angles of the four control surfaces.

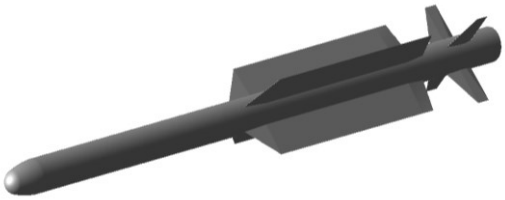

Figure 3 – Model of IRIS-T missile

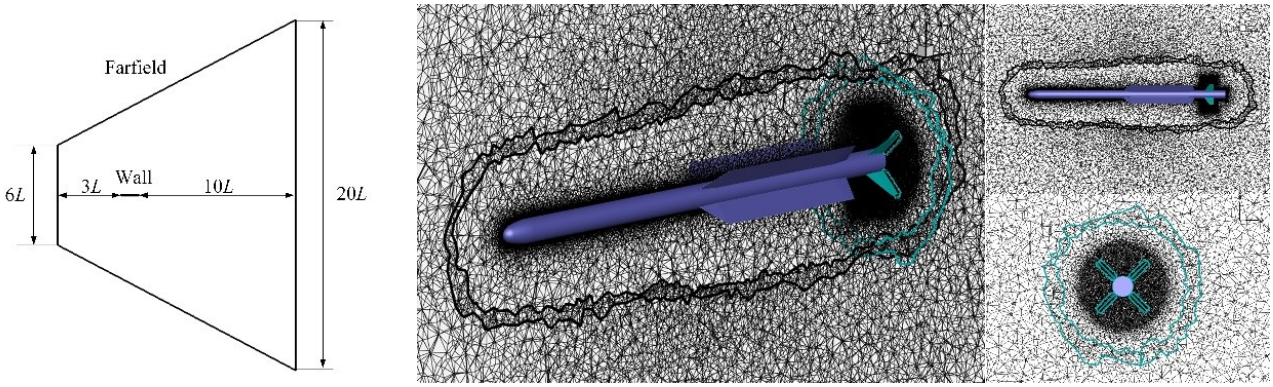

Figure 4 – Grid division of IRIS-T missile

4.1 High angle of attack pull-up maneuver numerical virtual flight

Flight control controls IRIS-T missile to carry out pull-up maneuver from 0° angle of attack to 20° angle of attack. The pull-up process lasts for 1.6s. The variation of the angle of attack of the missile control target over time is shown in the formula:

$$\begin{cases} \alpha(t) = \alpha_0 + \alpha_m \sin(\omega t), 0 \le t \le t_1 \\ \alpha(t) = \alpha_0 + \alpha_m, t > t_1 \end{cases} \tag{6}$$

Where, $\alpha_0=0, \alpha_m=20, t_1=1.6, \omega=5\pi/3$.

The results are presented in Figure 5, which displays the variation curves of the aircraft's angle of attack and elevator deviation angle, as well as longitudinal aerodynamic force, moment, and pitch velocity during the pull-up process from 0° to 20°. The missile's angle of attack rapidly increases with continuous upward deflection of the control surface during pulling up. The pitch angle velocity exhibits a trend of rapid increase followed by gradual decrease. Both lift coefficient and drag coefficient gradually increase with increasing angle of attack while pitch moment coefficient oscillates around zero. At t=1.6s, the angle of attack reaches 99.995% of its target value and elevator deviation angle stabilizes accordingly. As approaching the target value, both pitch moment coefficient and pitch angle velocity exhibit decreasing oscillation amplitude around zero while lift coefficient and drag coefficient converge to stable values.

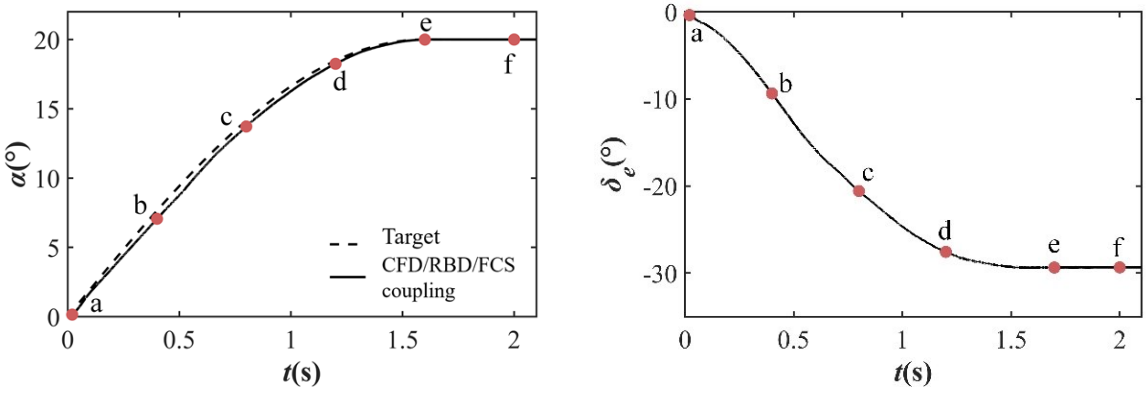

(a) Angle of attack (b) Elevator deviation angle

Figure 5 – Response curves of angle of attack and elevator deviation angle during 0° to 20° angle of attack pull-up

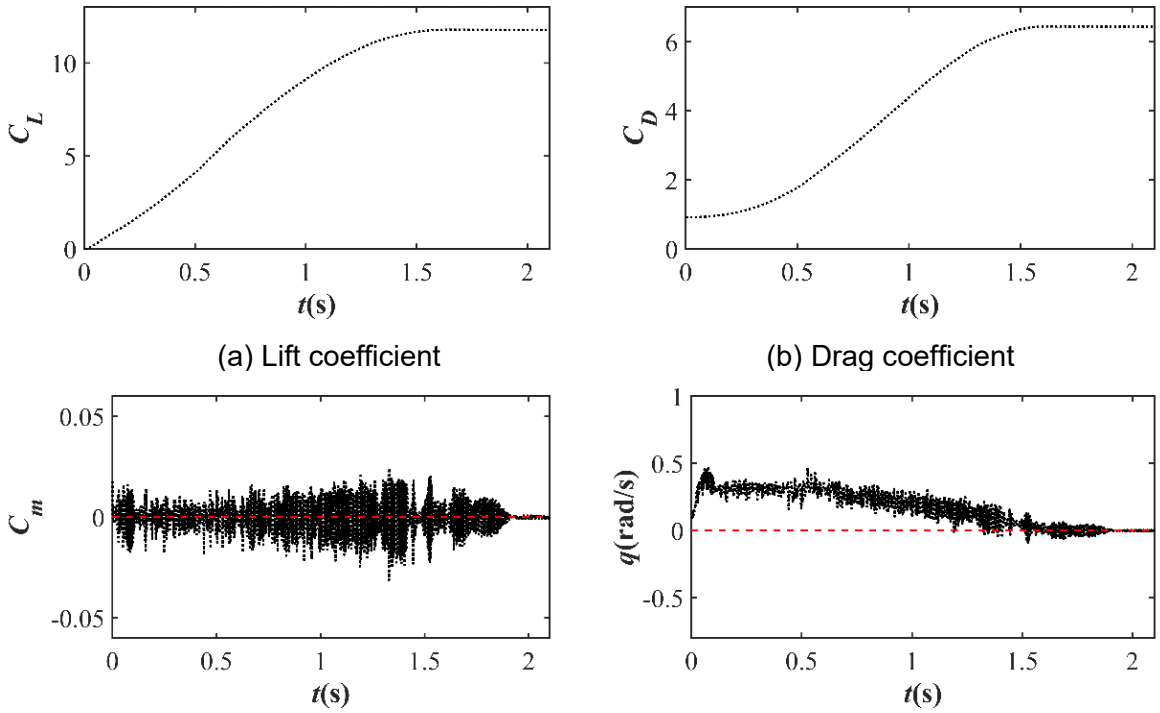

(a) Lift coefficient (b) Drag coefficient

(c) Pitch moment coefficient (d) Pitch angle velocity

Figure 6 – Longitudinal aerodynamic force and moment as well as pitch velocity changes in the process of 0° to 20° angle of attack

During the pull-up process, six state points a~f were selected. The figure illustrates the symmetry plane and surface flow field structure corresponding to each point. As depicted in Figure 7, from the initial moment to 1.6s, with the upward deflection of the elevator, the aircraft angle of attack is pulled up according to the sine function control input, and the included angle between the elevator and the incoming flow is always negative. Therefore, the pressure on the surface of elevator keeps increasing, while the pressure on the lower surface decreases, resulting in the upward torque, which increases the angle of attack and expands the high pressure area on the lower surface of the missile. The pressure coefficient on the upper surface decreases, especially at the wing position. However, from 1.6s to 2s, the missile's angle of attack changes slightly, so the surface pressure coefficient is basically unchanged. For Mach number cloud image, when t=0.02s, the head of the missile has a strong shock wave, and the wing and tail also have a shock wave. As the angle of attack increases, at t=0.4s, the shock wave on the windward side gradually approaches the wall and its intensity increases, while the shock wave on the leeward side gradually moves away from the wall. The shock wave generated at the turning point of the warhead and the projectile body intersects with the shock wave at the wing. At t=0.8s, the head shock wave of the windward side is close to the wall and converges with the shock wave of the projectile wing. Then, as the angle of attack continues to increase, the shock wave on the windward side keeps approaching the wall, while the shock wave on the lee side keeps away from the wall. From 1.2s to 1.6s, the flow field structure basically tends to be stable with little change.

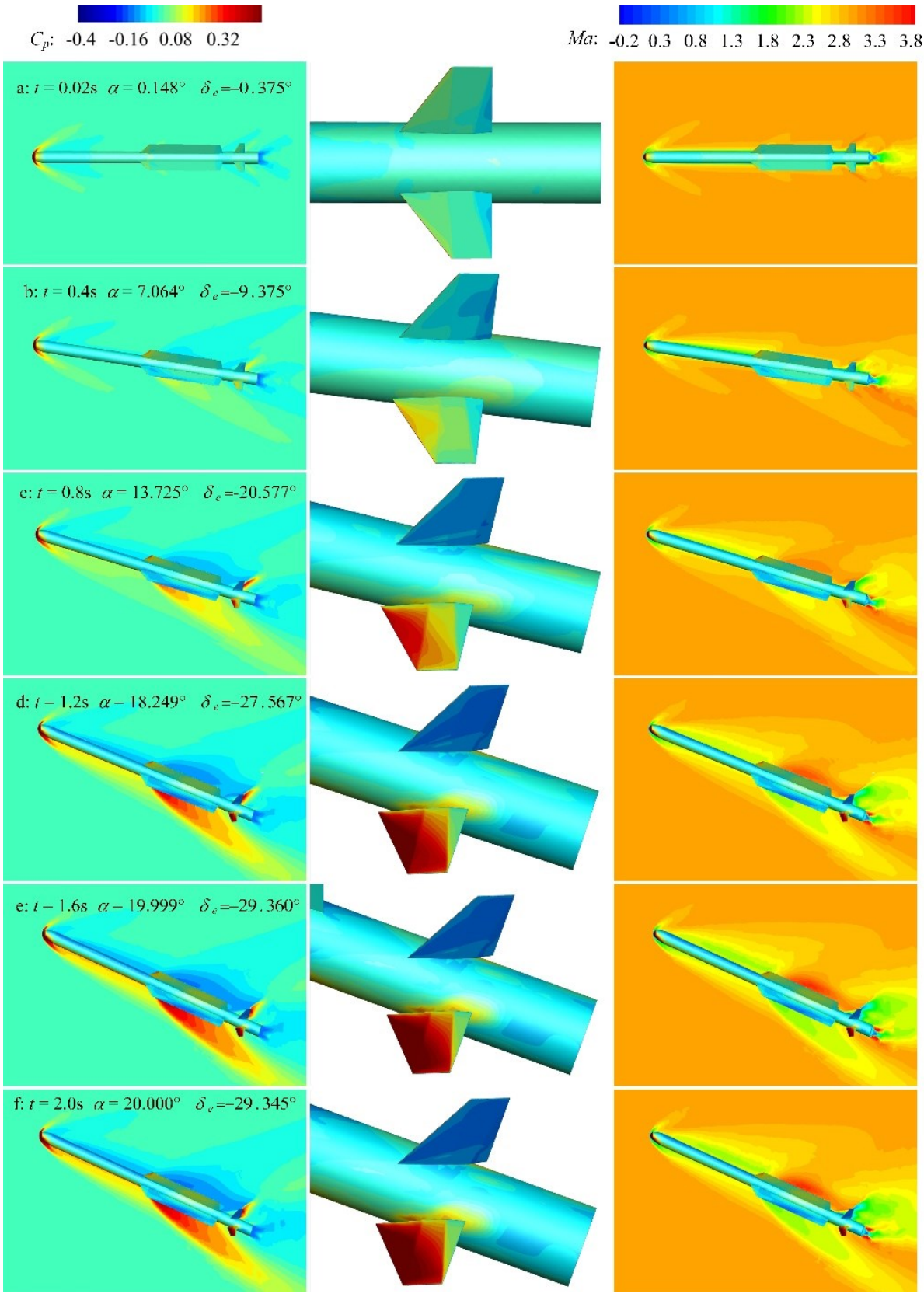

Figure 7 – Flow field of aircraft surface and plane of symmetry in the process of 0° to 20° angle of attack

4.2 Roll maneuver numerical virtual flight

The flight control system controls IRIS-T missile to maneuver from 0° to 5° with a time step of 0.0005s.

The maximum deflection rate of the limited control surface is 30°/s, and the pulling process lasts 0.16s. The variation of the angle of attack of the missile control target over time is shown in the formula:

$$\phi(t) = \phi_m \tag{7}$$

Where, ϕ_m=5.

The results are presented in the figure below, where Figure 8 illustrates the temporal variation of roll angle and control surface angle during the rolling process of the missile, while Figure 9 depicts the changes in lateral force coefficient, roll moment coefficient, pitch moment coefficient, and roll angle velocity. It can be observed that at the initial stage of rolling, there is a rapid upward deflection of the left control surface accompanied by a downward deflection of the right control surface, generating a rolling torque and increasing both roll angle speed and magnitude. Subsequently, as time progresses, there is a gradual downward deflection of the left control surface along with an upward deflection of the right control surface leading to a decrease in both rolling moment and roll angle speed. At t = 0.169 s, when reaching within ±2% error band for roll angle deviation from target value, both control surfaces gradually stabilize their positions while exhibiting small oscillations near zero for roll moment coefficient; meanwhile maintaining zero rate for roll angle velocity; furthermore, achieving stability for lateral force coefficient. Throughout this process influenced by rolling motion dynamics, slight variations are also observed in pitching moment coefficient which eventually converges towards a stable value. Moreover, upon comparison with pitch motion control process it becomes evident that adjustment time required for controlling roll motion is significantly shorter than that needed for pitch motion response resulting in faster overall response speed.

The pressure distribution of the missile surface and longitudinal symmetric plane during rolling motion is illustrated in Figure 10. From the initial moment to 0.01s, the left control surface exhibits an upward deflection, resulting in a slight decrease in the lower surface pressure coefficient of the left control surface. Simultaneously, the right control surface deflects downward, leading to an increase in the lower surface pressure coefficient and consequently generating a rolling moment that enhances the rolling angle of the missile. Subsequently, continuous downward deflection of the left control surface and upward deflection of the right control surface occur. This causes a reduction in rolling moment and deceleration in change speed of the rolling angle. Ultimately, as a result of these changes, both flow field structure and rolling angle tend towards stability.

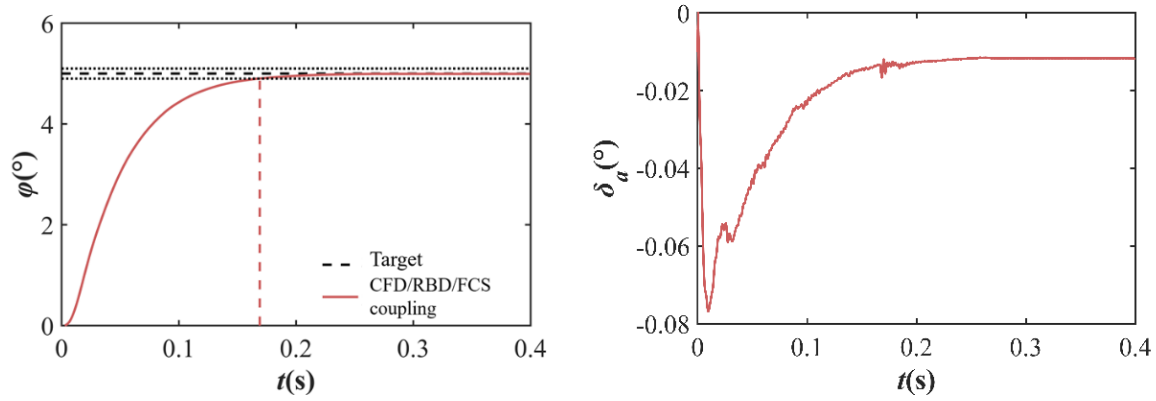

(a) Roll angle (b) Control surface deviation angle

Figure 8 – Change curves of roll angle and control surface deviation angle

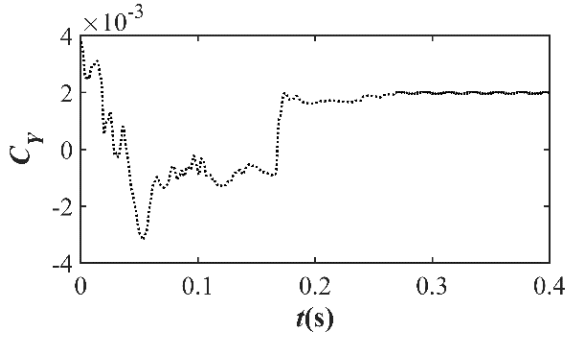

(a) Side force coefficient

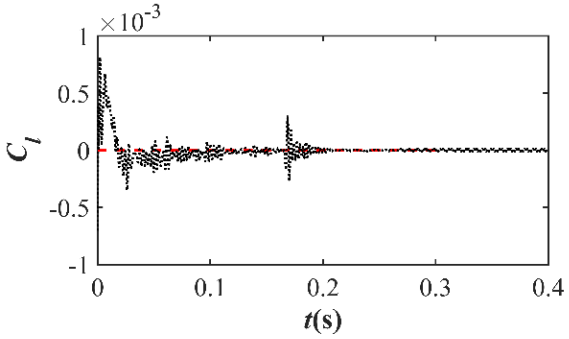

(b) Rolling moment coefficient

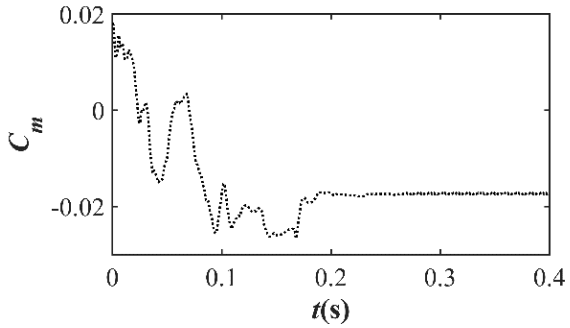

(c) Pitching moment coefficient

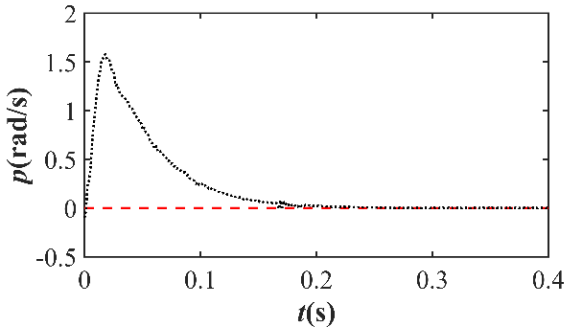

(d) Rolling angle velocity

Figure 9 – Variation curves of aerodynamic force, torque and rolling angle velocity during rolling

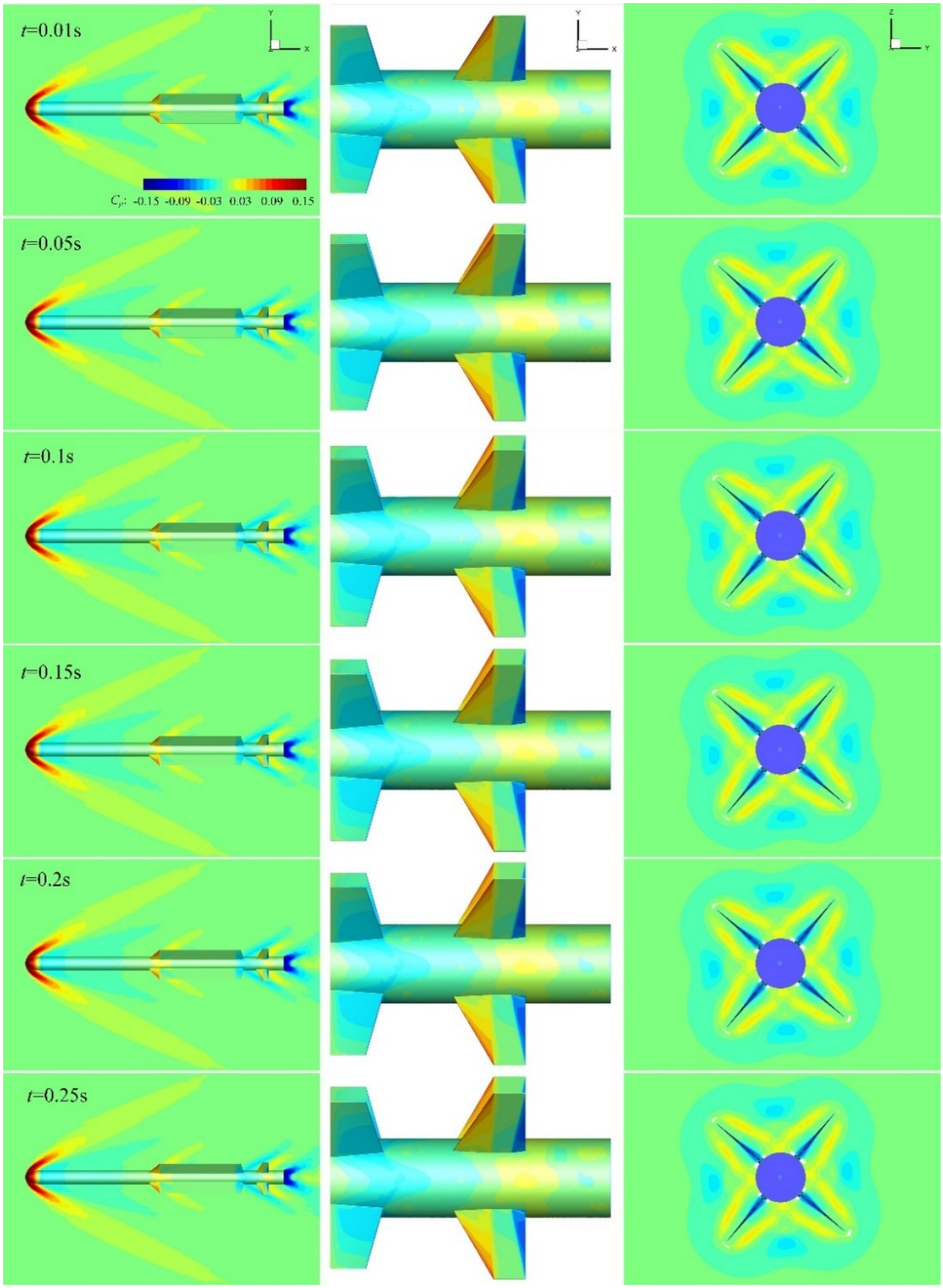

Figure 10 – Pressure coefficient changes of missile surface, symmetrical surface and control surface during rolling

5. Conclusion

This paper presents a numerical simulation method for the aerodynamic-motion-control integrated

coupling of high maneuvering aircraft, utilizing advanced technologies including unsteady flow numerical solution, dynamic unstructured nested grid technology, six-degree-of-freedom motion equation numerical solution, and flight control system design. A virtual flight simulation platform is developed to analyse the pitch and roll motion of an IRIS missile model under closed-loop control. The study sequentially simulates and analyses the static aerodynamic characteristics, forced oscillation motion, and free oscillation motion of the missile. Furthermore, a transfer function between aircraft attitude angle and control surface deflection angle is established to design a PID controller. By adjusting the PID parameters, a numerical simulation of high angle of attack pull-up process is conducted. The closed-loop attitude response characteristics, aerodynamic properties, and flow field changes during this process are analysed comprehensively. Additionally, the closed-loop response characteristics of missile roll angle in roll motion are simulated and analysed.

6. Contact Author Email Address

Mail to: qiaohongyu@nuaa.edu.

7. Copyright Statement

References

[1] William Lewis. Ucav: The next generation air-superiority fighter, 2012.

[2] Min Huang and Zhong wei Wang. A review of wind tunnel based virtual flight testing techniques for evaluation of flight control systems. *International Journal of Aerospace Engineering*, 2015:1-22, 2015.

[3] F Lawrence and B Mills. Status update of the aedc wind tunnel virtual flight testing development program. In *40th AIAA Aerospace Sciences Meeting Exhibit*, 2002.

[4] M Lowenberg and H Kyle. Development of a pendulum support rig dynamic wind tunnel apparatus. In *AIAA atmospheric flight mechanics conference and exhibit*, 2002.

[5] F. Zuniga, S. Cliff, D. Kinney, et al. Vehicle design of a sharp ctv concept using a virtual flight rapid integration test environment. In *AIAA Atmospheric Flight Mechanics Conference and Exhibit*, 2002.

[6] Paul Weinacht. Coupled cfd/gn&c modeling for a smart material canard actuator. 2004.

[7] M. R. Allan, Ken J. Badcock, and Bryan E. Richards. Cfd based simulation of longitudinal flight mechanics with control. 2005

[8] Bradford E. Green, Ryan Czerwiec, Theresa C. Shafer, and Mackenzie Rhinehart. Cfd predictions of the stability and control characteristics of the e-2d advanced hawkeye. *2018 Applied Aerodynamics Conference*, 2018.

[9] Norbert Kroll, Mohammad Abu-Zurayk, Diliana Dimitrov, Thomas Franz, Tanja Führer, Thomas Gerhold, Stefan Görtz, Ralf Heinrich, aslav Ilić, Jonas Jepsen, Jens Jägersküpper, Martin Kruse, Andreas Krumbein, Sabine C. Langer, D. Liu, René Liepelt, Lars Reimer, Markus Raimund Ritter, Axel Schwöppe, Julian Scherer, Frank Spiering, Reik Thormann, V. Togiti, Daniel B. Vollmer, and Jan-Hendrik Wendisch. Dlr project digital-x: towards virtual aircraft design and flight testing based on high-fidelity methods. *CEAS Aeronautical Journal*, 7:3-27, 2016.

[10] Jubaraj Sahu and Frank E. Fresconi. Flight behaviors of a complex projectile using a coupled computational fluid dynamics (cfd)-based simulation technique: Free motion. 2015.

[11] Jubaraj Sahu and Frank Fresconi. Flight behaviors of a complex projectile using a coupled cfd-based simulation technique: Open-loop control. *In 54th AIAA Aerospace Sciences Meeting*. American Institute of Aeronautics and Astronautics, 2016. Clinton J. Ratcliff, David J. Bodkin, James Clifton, and M. C. Willis. Virtual flight testing of high performance fighter aircraft using high-resolution cfd. 2016.

[12] Ratcliff C J, Bodkin D J, Clifton J, et al. Virtual Flight Testing of High Performance Fighter Aircraft Using High-Resolution CFD. *AIAA Atmospheric Flight Mechanics Conference*. 2016.

[13] Tianhang Xiao, Haolin Zhi, Shuanghou Deng, Zhao Jun Chen, and Xinying Li. Enhancement on parallel

unstructured overset grid method for complex aerospace engineering applications. *Chinese Journal of Aeronautics*, 2022.

[14]B.L. Stevens, F.L. Lewis, and E.N. Johnson. *Aircraft Control and Simulation*. Wiley-Interscience, 2016.